UV-NIR efficiency of the refractive index matching mechanism on colorectal muscle during treatment with different glycerol osmolarities

Nelma Gomes[1], Valery V. Tuchin[2,3,4], and Luís M. Oliveira[1,5*]

[1] Department of Physics, Polytechnic of Porto – School of Engineering, 431 Rua Dr. António Bernardino de Almeida, Porto 4249-015, Portugal

[2] Research-Educational Institute of Optics and Biophotonics, Saratov State University, 83 Astrakhanskaya str., Saratov 410012, Russia

[3] Laboratory of Laser Diagnostics of Technical and Living Systems, Institute of Precision Mechanics and Control of the Russian Academy of Sciences, 24 Rabochaya str., Saratov 410028, Russia

[4] Interdisciplinary Laboratory of Biophotonics, Tomsk State University, 36 Lenin Ave., Tomsk 634050, Russia

[5] Centre of Innovation in Engineering and Industrial Technology, 431 Rua Dr. António Bernardino de Almeida, Porto 4249-015, Portugal

*** e-mail:** lmo@isep.ipp.pt

Abstract. The evaluation of the optical clearing mechanisms in tissues provides information about the efficiency of the clearing treatment. One of such mechanisms is the refractive index matching, which is created by the partial replacement of tissue water by an optical clearing agent with higher refractive index, better matched to the index of tissue scatterers. With the objective of evaluating the refractive index matching mechanism for a wide spectral range and comparing its magnitude between treatments with different clearing agent osmolarities, thickness and collimated transmittance measurements were obtained from human colorectal muscle samples under treatment with 20%-, 40% and 60%-glycerol. Such measurements were used in a calculation model to obtain the refractive index kinetics for the interstitial fluid and for the whole tissue. The calculation results show that the refractive index matching has a stronger effect in the ultraviolet and that such matching is more effective for higher agent concentrations in the treating solutions. © 2020 Journal of Biomedical Photonics & Engineering.

Keywords: ultraviolet spectroscopy; refractive index matching; light scattering; tissue water content; optical clearing; colorectal muscle; collimated transmittance.

Paper #3374 received 25 May 2020; revised manuscript received 12 Jun 2020; accepted for publication 14 Jun 2020; published online 26 Jun 2020. doi: 10.18287/JBPE20.06.020307.

1 Introduction and theoretical background

Since its rediscovery about 30 years ago [1], the research related to the Optical immersion Clearing (OC) technique has produced a large number of publications [2], which continues to grow significantly. Some of those studies were made to evaluate, discriminate and characterize the mechanisms of OC [2–8], while others evaluated the diffusion properties of the optical clearing agents (OCAs) in tissues [9–16], or described such diffusion as a molecular-based model [17–18].

The combination of OC treatments with other optical-based methods in clinical practice provides significant improvements, since by reducing light scattering inside tissues, it allows for higher tissue-depth optical probing and imaging, higher contrast and resolution in diagnostic images [19–26]. Some imaging and spectroscopy studies made during OC treatments have allowed to discriminate between normal and pathological tissues. One of those spectroscopy studies was reported by Carvalho et al. [16], where colorectal

cancer was identified by evaluating the different content of mobile water in normal and pathological tissues. Imaging methods have also been applied to identify tumor locations in tissues after clearing [19, 21–23]. One of such studies was reported by Lagerweijt et al. [26], where fluorescence confocal imaging, two-photon imaging, photoacoustic imaging and image reconstruction of optically cleared tissues have allowed to discriminate between normal and infiltrating glioblastoma brain tumors in rats.

As a result of OC evaluation and characterization studies, it is known that tissue transparency increases during treatments as a result of three major mechanisms, commonly designated as: tissue dehydration, refractive index (RI) matching and protein dissociation [2, 27–30]. Tissue dehydration occurs when interstitial water flows out as a result of the osmotic pressure that the OCA creates inside the tissue. Such water flux leads to a more compact and better organized distribution of the other tissue components (scatterers) [2]. As the water flows out, the OCA, with a higher RI, flows into the interstitial locations to partially replace the leaving water and provide the RI matching mechanism [3]. Considering that water, tissue scatterers and OCAs have a decreasing behavior with increasing wavelength [2, 31–34], it is expected that the RI matching will have a higher effect on scattering in the ultraviolet (UV) range. The third OC mechanism, designated as protein dissociation, has also been observed as a result of the interaction of the OCA molecules with protein connections [27]. Since proteins have a strong absorption band in the deep-UV (200–230 nm) [31, 35–36], such dissociation also leads to a higher RI matching in this wavelength range. Such fact was recently reported by Carneiro et al. [37], where two OC-induced transparency windows were observed in the UV, with central peaks at 230 and 300 nm. This study also demonstrated that the magnitude of these windows increases with the OCA concentration in the treating solution [37], which suggests that higher OCA concentrations provide a higher magnitude RI matching in the UV range.

It has been demonstrated that all the three OC mechanisms are completely reversible, provided that the OCA is later washed out by subsequent tissue rehydration [2, 27, 38]. Such rehydration occurs naturally *in vivo*, since water from adjacent areas of the tissue flows into the treated area and the OCA is completely expelled out [2]. For the *ex vivo* situation, washing out of the OCA can be provided by immersing the treated tissue in saline.

Tissue spectroscopy is a powerful tool in the study of OC treatments, since it provides data for a wide spectral range. One of the benefits of using sensitive spectroscopy measurements from tissues during OC treatments for a range between the UV and the near infrared (NIR), is that comparison of the induced variations can be made between the UV, visible and NIR.

In a previous study by our group [39], we have evaluated the RI matching mechanism in the visible-NIR range in skeletal muscle under treatment with glucose and ethylene glycol solutions, showing that both the RI of the interstitial fluid (ISF) and of the whole tissue increase as a result of the applied OC treatments.

With the objective of studying the RI matching mechanism and compare its magnitude between the UV, visible and NIR ranges, the present study was conducted with human colorectal muscle under treatment with different glycerol osmolarities.

2 Materials and methods

The present study consisted only of the calculation of the RI matching mechanism in human colorectal muscle for a wide spectral range during treatments with glycerol in different osmolarities. The samples and collimated transmittance (T_c) measurements used in these calculations are the same that were used in a previous study that reported the discovery of two OC-induced tissue windows in the UV range [37]. Sub-section 2.1 presents a resumed description of tissue collection, sample preparation and measurement procedure, which were used in that study. The following sub-sections describe the calculation procedure adopted to obtain the RI kinetics of colorectal muscle during treatments.

2.1 Tissue samples and measurement procedure

The tissue samples used to obtain the measurements necessary for this study were obtained from surgical resections of patients under treatment at the Portuguese Oncology Institute of Porto, Portugal. The collection of surgical resections and sample preparation were performed according to the guidelines of the Ethics Committee of that Institution and after obtaining a written consent from the patients to use surgical specimens for diagnostic and research purposes.

The muscle layer of the colorectal wall was retrieved from the surgical resections and a cryostat (Leica Biosystems, model CM 1850 UV) was used to prepare the samples for the study with approximate circular slab-form, having diameter $\phi = 1$ cm and 0.5 mm thickness.

Three of these samples were submitted to T_c measurements during the OC treatments with aqueous solutions containing 20%-, 40%- or 60%-glycerol (one sample per treatment) [37]. The setup to perform T_c measurements is presented in Fig. 1 of Ref. [37], where an optical fiber cable delivers a collimated beam of 1 mm from a broadband light source into a cuvette that contains the tissue sample. A similar optical fiber collects the collimated transmitted beam to deliver it to the spectrophotometer. For measurements during treatment, the solution is introduced inside the cuvette to immerse the sample. The volume of the solution is about 10× higher than the sample volume to guarantee a continuous flux of the OCA into the tissue during the treatment. The samples used in the study of Ref. [37]

had low blood content, which resulted in low magnitude for the absorption bands of hemoglobin. To obtain more realistic results in the present study, ten other muscle samples, from which we recently measured the native T_c spectra and presented well-defined Soret and Q-bands, were used to perform calculations.

Thickness measurements were also made during treatment with the same glycerol solutions, using a precision micrometer as described in Fig. 1B of Ref. [39]. Nine muscle samples were used in these measurements, three per treatment with each glycerol osmolarity, to obtain more precise mean thickness kinetics.

2.2 Recovery of T_c kinetics

Since we had previously measured kinetics data for the T_c spectra during the treatments with various glycerol osmolarities to use in the study reported in Ref. [37], we needed to retrieve the time dependence variations created by those treatments to use in the calculations of the RI kinetics intended for the present study.

As indicated above, the T_c kinetics reported in Ref. [37] were obtained from muscle samples with low blood content. Since we intended to present more realistic results, for tissues that have some absorption bands, and to show the effect of such bands in tissue dispersion and following kinetics, we needed to adjust the previous T_c kinetics [37] to tissues that had such spectral signatures.

The recovery of the T_c kinetics and their recalculation for treatments with more realistic tissues was made in the following way for each treatment:

I. In the study presented in Ref. [37], the OC efficiency was calculated as:

$$\mathrm{OC}_{eff}\left(\lambda,t\right)=\frac{T_c\left(\lambda,t\right)-T_c\left(\lambda,t=0\right)}{T_c\left(\lambda,t=0\right)}\times 100\%, \quad (1)$$

where $T_c(\lambda, t = 0)$ represents the spectrum of the untreated sample and $T_c(\lambda, t)$ represents the spectrum measured at each time of treatment t. The resulting $\mathrm{OC}_{eff}(\lambda, t)$ contains information about the T_c variations for colorectal muscle in each treatment, which can be retrieved to use with other native T_c spectrum from the same tissue under the same OC treatments.

II. Using recent T_c spectra, which were measured from similar colorectal muscle samples that had higher blood content and better-defined hemoglobin bands, we calculated the mean and standard deviation (SD) for the native $T_c(\lambda)$ of the muscle. The calculated mean $T_c(\lambda)$ for the native muscle was used in Eq. (2) as a replacement of $T_c(\lambda, t = 0)$ to calculate the time dependence variations in $T_c(\lambda)$:

$$T_c\left(\lambda,t\right)=\frac{\mathrm{OC}_{eff}\left(\lambda,t\right)\times T_c\left(\lambda,t=0\right)}{100\%}+T_c\left(\lambda,t=0\right). \quad (2)$$

This means that the $T_c(\lambda, t)$ spectra obtained with this calculation for each treatment contains the same spectral signatures for hemoglobin as the recent measured samples and the corresponding kinetics that were obtained by measurement in the study of Ref. [37]. As a result, using this data will produce more realistic RI kinetics data.

2.3 Calculation of optical properties for the native colorectal muscle

To perform the calculations to obtain the RI kinetics for each treatment, it was also necessary to obtain the optical properties of the untreated tissue, namely the absorption coefficient ($\mu_a(\lambda)$), the scattering coefficient ($\mu_s(\lambda)$) and tissue dispersion ($n_{\mathrm{muscle}}(\lambda)$).

The calculation of these properties was performed according to the following procedure:

I. Using the sample thickness (d = 0.5 mm) and the mean $T_c(\lambda)$ that was obtained from the recent measurements, we calculated the attenuation coefficient ($\mu_t(\lambda) = \mu_a(\lambda) + \mu_s(\lambda)$) using the Bouguer-Beer-Lambert equation [40]:

$$\mu_t\left(\lambda,t=0\right)=\frac{-\ln\left(T_c\left(\lambda,t=0\right)\right)}{d}. \quad (3)$$

II. The wavelength dependence for μ_s is described in literature [41] as a combination of Rayleigh and Mie scattering regimes:

$$\mu_s\left(\lambda\right)=a'\times\left(\begin{array}{l} f_{\mathrm{Ray}}\times\left(\dfrac{\lambda}{500(\mathrm{nm})}\right)^{-4}+ \\ +\left(1-f_{\mathrm{Ray}}\right)\times\left(\dfrac{\lambda}{500(\mathrm{nm})}\right)^{-b_{\mathrm{Mie}}} \end{array}\right), \quad (4)$$

where a' is a multiplying factor that establishes the magnitude of μ_s at 500 nm, λ is the wavelength (nm), f_{Ray} is the Rayleigh scattering fraction and b_{Mie} represents the decreasing power for the Mie scattering component [41].

After obtaining the optimal curve for $\mu_s(\lambda)$ through Eq. (4), with appropriate estimated values for a', f_{Ray} and b_{Mie}, we subtracted it to $\mu_t(\lambda)$ to obtain $\mu_a(\lambda)$.

III. After obtaining the wavelength dependence for μ_a, we could calculate the dispersion for the colorectal muscle. Refs. [42–43] describe a set of transformation relations to obtain the real and imaginary parts of the RI from the optical properties of a medium. Such relations are known as the Kramers-Kronig (K-K) relations. The relation to calculate the real part of the RI, which is the one we need, is described as [42–43]:

$$n_{\mathrm{muscle}}\left(\lambda\right)=1+\frac{2}{\pi}\int_0^{\infty}\frac{\lambda}{\Lambda}\cdot\frac{\lambda}{\Lambda^2-\lambda^2}\kappa\left(\lambda\right)\mathrm{d}\Lambda, \quad (5)$$

where Λ represents the integrating variable over a wavelength spectral range under consideration and λ is a fixed wavelength in that range that can be tuned for better adjustment of the calculated dispersion. κ(λ) represents the imaginary part of the RI, which can also be calculated by another K-K relation [42–43], or in a simpler way if we have $\mu_a(\lambda)$ [42]:

$$\kappa(\lambda)=\frac{\lambda}{4\pi}\mu_a(\lambda). \quad (6)$$

Since we have already calculated $\mu_a(\lambda)$, we used it in Eq. (6) to obtain κ(λ) for the range between 200 and 1000 nm, which was then used in Eq. (5) to calculate $n_{muscle}(\lambda)$ for the same range. To check the accuracy of this calculation, we compared $n_{muscle}(\lambda)$ with the previous dispersion that we have calculated form direct RI measurements at different wavelengths in the visible-NIR range [44]. Both curves matched perfectly in the visible-NIR range, showing differences only in the UV range, where significant absorption bands occur and where we had no experimental RI data to use in the previous estimation. Such agreement indicates that the dispersion estimation from K-K relations is good and more precise in the UV range.

2.4 Calculation of tissue dispersion kinetics

Once we have obtained all the necessary optical properties for the native muscle and the kinetics measurements for thickness and T_c during the treatments, we could calculate the RI kinetics for the colorectal muscle and for its ISF, according to a model described in literature [39, 44–46].

Such model considers that for short-time treatments the OCA will only partially replace the interstitial water, without any interaction with the scatterers, meaning that the scatterers will keep their hydration, RI and absolute volume [45]. Due to this fact, the RI of tissue scatterers ($n_{scat}(\lambda)$), which remains unchanged during treatment, needs to be calculated. Such calculation was previously made [44], based on experimental RI data obtained at wavelengths within the visible-NIR range. To get more realistic data that accounts for the wide spectral range between 200 and 1000 nm, we performed a simple calculation. The ISF is known to be composed mainly by water and some dissolved salts, proteins and minerals [2, 45, 47–48]. This way, the wavelength dependence for its RI ($n_{ISF}(\lambda)$), can be described as a combination of the dispersions of water ($n_{H2O}(\lambda)$) and dry matter (completely dehydrated muscle, $n_{dry}(\lambda)$), through the Gladstone and Dale equation [39, 44–47, 49–54]:

$$\begin{aligned} &n_{ISF}(\lambda)=f_{H_2O}\times n_{H_2O}(\lambda)+f_{dry}\times n_{dry}(\lambda);\\ &f_{H_2O}+f_{dry}=1. \end{aligned} \quad (7)$$

To perform such calculation, it was first necessary to obtain $n_{dry}(\lambda)$. Assuming that the total water content in colorectal muscle is 73%, which is a similar value to the total water in neighbor tissues of the colorectal wall [46], we used the Gladstone and Dale equation to calculate $n_{dry}(\lambda)$:

$$n_{dry}(\lambda)=\frac{n_{muscle}(\lambda)-f_{H_2O}\times n_{H_2O}(\lambda)}{1-f_{H_2O}}, \quad (8)$$

where f_{H2O} was replaced by 0.73, $n_{muscle}(\lambda)$ was calculated by Eq. (5) and $n_{H2O}(\lambda)$ represents the water dispersion between 200 and 1000 nm as reported for 20 ºC [55].

Finally, to obtain $n_{scat}(\lambda)$, the same equation can be applied for the entire tissue, using the volume fractions (VFs) for the ISF and scatterers [44]:

$$n_{scat}(\lambda)=\frac{n_{muscle}(\lambda)-f_{ISF}\times n_{ISF}(\lambda)}{1-f_{ISF}}, \quad (9)$$

where f_{ISF} is the VF of the ISF, $1-f_{ISF}$ is the VF of scatterers (f_{scat}) and $n_{ISF}(\lambda)$ is calculated with Eq. (7). Since we know from previous study [44] that $f_{ISF}=0.6$ and $f_{scat}=0.4$, all these calculations can be made, ultimately depending on the values of f_{H2O} and f_{dry} in Eq. (7), which are unknown. When performing calculations with Eq. (7) we tried some combinations for these VFs in Eq. (7) and for the combination with $f_{H2O}=84\%$ and $f_{dry}=16\%$, the calculated dispersions for the ISF and scatterers matched the ones we previously calculated based on experimental RI data in the visible-NIR range. These graphs are presented in Section 3.

The following step consisted on calculating the kinetics for the VFs. Since the scatterers keep their absolute volume unchanged, we started by calculating it from the untreated sample volume ($V_{sample}(t=0)$) [39]:

$$V_{scat}=V_{sample}(t=0)\times f_{scat}(t=0)\ \text{cm}^3, \quad (10)$$

where $f_{scat}(t=0)$ is 0.4. The untreated sample volume was calculated considering the sample slab-form radius ($\phi=1$ cm) and thickness ($d=0.5$ mm) as:

$$V_{sample}(t=0)=(\pi\times 0.5^2)\times 0.05\ \text{cm}^3. \quad (11)$$

Since V_{scat} does not change during treatment, but V_{sample} will change, we calculated the time dependence for f_{scat} considering the variations in sample thickness ($d(t)$) as:

$$f_{scat}(t)=\frac{V_{scat}}{(\pi\times 0.5^2)\times d(t)}. \quad (12)$$

Since from Gladstone and Dale law (Eq. (7)), the sum of VFs equals 1, we could calculate $f_{ISF}(t)$ from

$f_{scat}(t)$.

The following step was to calculate the kinetics for the RI of the ISF that occurs due to the partial replacement of water by glycerol. Such partial replacement and consequent variations in the VFs will induce changes in the scatterer density (ρ_s) inside the sample. Since μ_s is the product between the scattering cross section (σ_s) and ρ_s [40], the following equation must be considered to determine the time dependence for n_{ISF} [2, 39, 44]:

$$\bar{n}_{ISF}(\lambda,t) = \frac{n_{scat}(\lambda)}{\left(\sqrt{\frac{\mu_s(\lambda,t)\times d(t)}{\mu_s(\lambda,t=0)\times d(t=0)}}\times\left(\frac{n_{scat}(\lambda)}{n_{ISF}(\lambda)}-1\right)+1\right)}, \quad (13)$$

where $n_{scat}(\lambda)$ is the dispersion of scatterers as calculated by the Gladstone and Dale law (Eq. (9)), $n_{ISF}(\lambda)$ is the dispersion of the ISF in the untreated tissue (calculated with Eq. (7)). Sample thickness for the untreated tissue and during treatment are represented as $d(t = 0)$ and $d(t)$, respectively, and $\mu_s(\lambda, t = 0)$ and $\mu_s(\lambda, t)$ are the wavelength dependencies for the scattering coefficient for the untreated tissue and during treatment. The calculation of $\mu_s(\lambda, t = 0)$ was made using Eq. (4) and its kinetics during treatment were obtained by subtracting the unchanged $\mu_a(\lambda)$ to the kinetics of μ_t, which were calculated from the thickness and T_c kinetics using Eq. (3). All the results from these calculations are presented in Section 3.

3 Results and discussion

Considering the various experimental steps described in Section 2, we will present sequential results in this section, starting with the experimental data and calculation of the optical properties for the untreated muscle in Sub-section 3.1. The results that correspond to the OC-induced variations will be presented in Sub-section 3.2

3.1 Tc measurements and calculated optical properties for the natural muscle

As indicated in Section 2, we have recently used 10 colorectal muscle samples to acquire precise T_c spectra that show well-defined absorption bands for hemoglobin. Such accuracy and spectral quality depends on the blood content of the samples, which sometimes is low. Figure 1 presents the mean T_c spectrum for the human colorectal muscle that resulted from these measurements. The error bars in Fig. 1 represent the SD obtained from the 10 measurements.

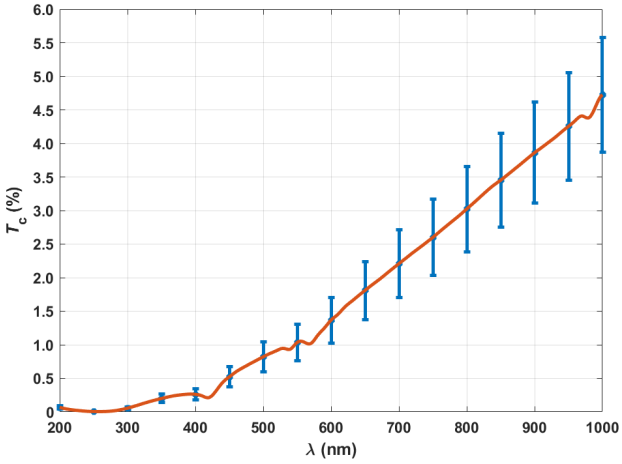

Fig. 1 Mean T_c spectrum of the human colorectal muscle.

As we can see from Fig. 1, T_c is very low in the UV range, and practically null between 200 and 300 nm. Considering the visible-NIR range, T_c increases almost linearly with wavelength, showing the absorption bands at 418 nm (Soret), 540 and 570 nm (Q-bands) and 980 nm (water).

Using the sample thickness of 0.5 mm and the mean spectrum presented in Fig. 1 in Eq. (3), we calculated $\mu_t(\lambda)$. Using the Curve Fitting Tool on MATLAB™, we recreated $\mu_s(\lambda)$ that better suits the calculated $\mu_t(\lambda)$. In this estimation for $\mu_s(\lambda)$, we used Eq. (4). Fig. 2 presents the calculated curves for $\mu_t(\lambda)$ and $\mu_s(\lambda)$.

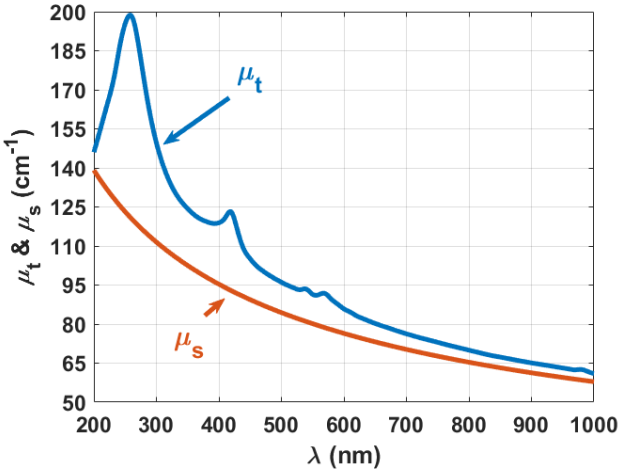

Fig. 2 Calculated $\mu_t(\lambda)$ and estimated $\mu_s(\lambda)$ for the native colorectal muscle.

The curve in Fig. 2 for $\mu_s(\lambda)$ is described as:

$$\mu_s(\lambda) = 84.41 \times \left(3.371 \times 10^{-5} \times \left(\frac{\lambda}{500(\text{nm})} \right)^{-4} + \right.$$
$$\left. + \left(1 - 3.371 \times 10^{-5}\right) \times \left(\frac{\lambda}{500(\text{nm})} \right)^{-0.5446} \right), \quad (14)$$

As we can see from Fig. 2, $\mu_s(\lambda)$ was constructed to be a little lower than $\mu_t(\lambda)$, so that the difference between the two represents $\mu_a(\lambda)$. After calculating such difference, we obtained $\mu_a(\lambda)$, which is presented in Fig. 3.

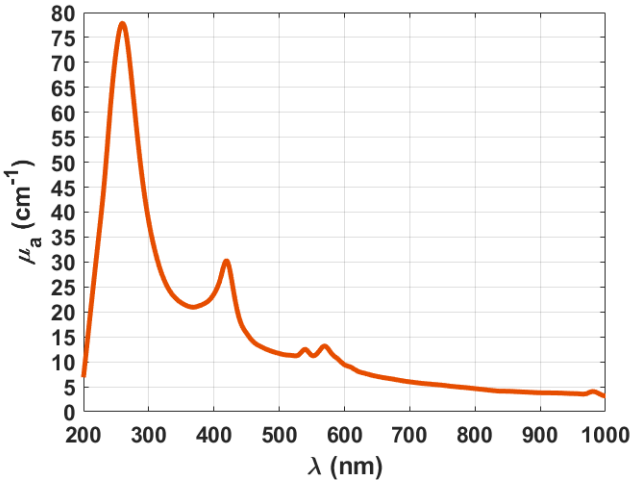

Fig. 3 $\mu_a(\lambda)$ for the native colorectal muscle.

The calculated $\mu_a(\lambda)$ presents the typical wavelength dependence for biological tissues and contains precise information about the main absorbers in the muscle. Fig. 3 shows the absorption band of DNA (260 nm), the Soret band (418 nm), the Q- bands (540 and 570 nm) and the absorption band of water (980 nm). With such detail in $\mu_a(\lambda)$ we see that the calculation through the BBL equation is precise, in opposition to traditional estimation methods, such as the inverse Adding-Doubling method, which is not able to detect absorption bands in the spectral range where scattering is strong (UV range) [31].

Using the data in Fig. 3, the muscle dispersion was calculated through K-K relations (Eqs. (5) and (6)). The result of this calculation and the previous smooth dispersion, which was calculated from experimental RI measurements in the visible-NIR range [44], are presented in Fig. 4 for comparison.

Both curves presented in Fig. 4 show good agreement in the visible-NIR range, but the one estimated through K-K relations provides more information, since it contains the spectral signatures of the major absorbers in the muscle. This curve was selected for further calculations.

The following step was to calculate the dispersions for the ISF and scatterers in the muscle. Such calculation procedure was made using Eqs. (7) to (9) and as described in Sub-section 2.4. The resulting dispersions are presented in Fig. 5, where the smooth dispersions, previously obtained [44], are also represented for comparison.

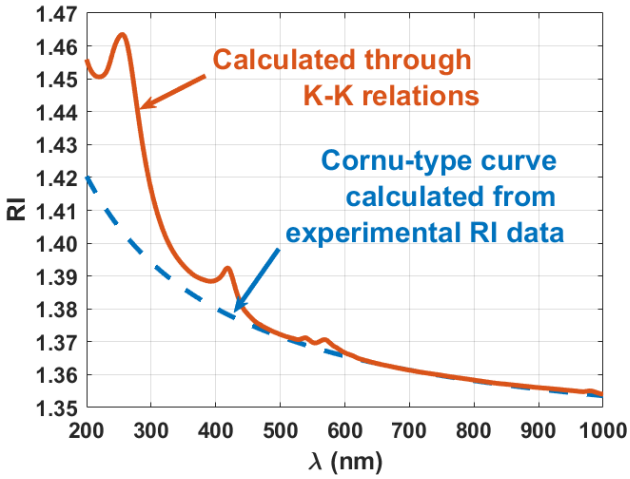

Fig. 4 Colorectal muscle dispersion curves.

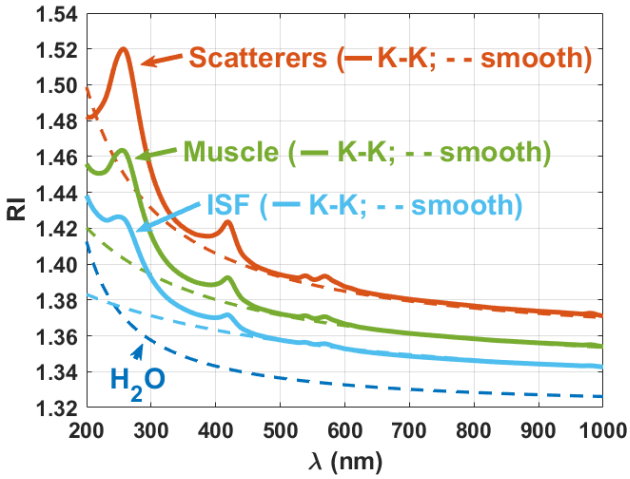

Fig. 5 Dispersion curves for the colorectal muscle and its components.

We can see from Fig. 5 that for the visible-NIR range, the dispersions calculated based on K-K relations have good agreement with their smooth correspondents. Such agreement indicates that such estimation for the dispersions of the ISF and scatterers is good and it provides more information about the spectral signatures that each dispersion has. As example, the K-K calculated dispersion for the ISF shows that ISF also contains some DNA and hemoglobin molecules – peaks at 260 and 418 nm. The content of these molecules is much stronger in scatterers, as expected, as seen by the magnitude of the peaks in the top dispersion in Fig. 5.

After obtaining the wavelength dependence for the optical properties that are necessary to calculate the dispersion kinetics, we will now present the results of such calculations.

3.2 Calculation of dispersion kinetics

After reconstructing the T_c spectra for all treatments from the OC efficiency data published in Ref. [37] and the mean T_c spectrum presented in Fig. 1, we initiated the calculations to obtain the dispersion kinetics.

The first step of this calculation was to obtain the kinetics for the VFs in each treatment. To perform such calculations, we used the mean thickness kinetics (mean of 3 studies for each treatment), presented in Fig. 6.

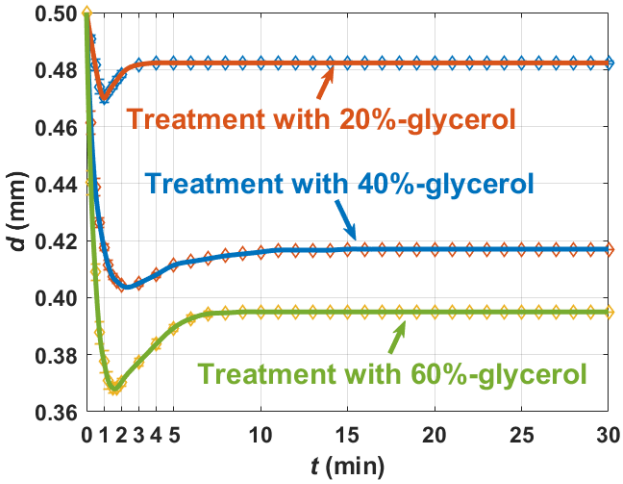

Fig. 6 Mean thickness kinetics during the treatments with 20%-glycerol, 40%-glycerol and 60%-glycerol.

The curves presented in Fig. 6 are smooth splines that were adjusted to the discrete experimental thickness data for each treatment. According to these curves, all treatments show a strong initial decrease of sample thickness, which is evidence of the fast dehydration mechanism. The magnitude of such thickness decrease rises with the glycerol concentration in the treating solution. After the initial thickness decrease, we see a smooth increase in sample thickness that lasts for different time intervals for each treatment. Such smooth increase is evidence of the OCA flux into the interstitial locations of the muscle to perform the RI matching mechanism. After that smooth increase, thickness stabilizes, showing that the effective net flux between the tissue and the treating solution has ended.

The mean data for each treatment in Fig. 6 was used in Eq. (12) to calculate $f_{scat}(t)$, which through the Gladstone and Dale law (Eq. (7)) allowed to calculate $f_{ISF}(t)$. The time dependence for the VFs in each treatment are presented in Fig. 7.

The graphs in Fig. 7 show that the major changes in the VFs occur within the first 5 min of treatment. The magnitude of these variations increases with the concentration of glycerol in the treatment solution and for the treatment with 60%-glycerol it indicates that $f_{scat}(t)$ grows above $f_{ISF}(t)$.

The calculated kinetics for the T_c spectra in each treatment also shows increasing behavior, as we can see from Fig. 8.

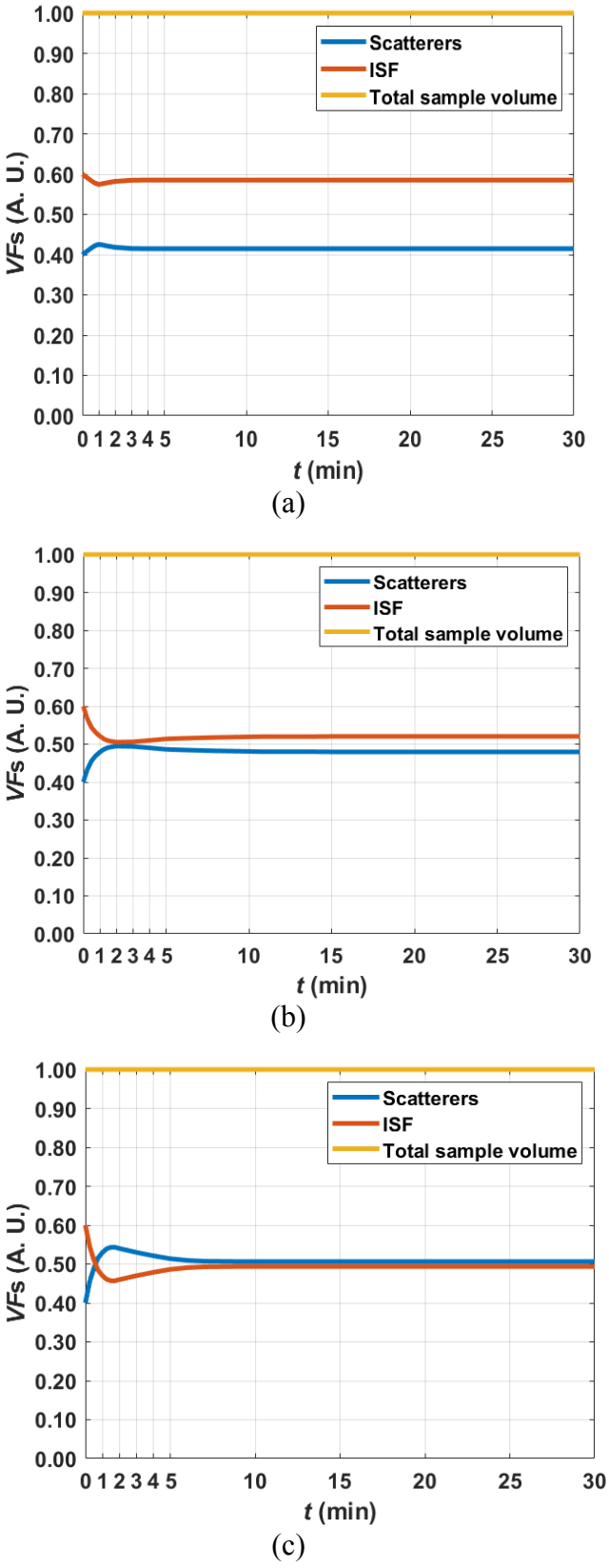

Fig. 7 Kinetics for the VFs for the treatments with: 20%-glycerol (a), 40%-glycerol (b) and 60%-glycerol (c).

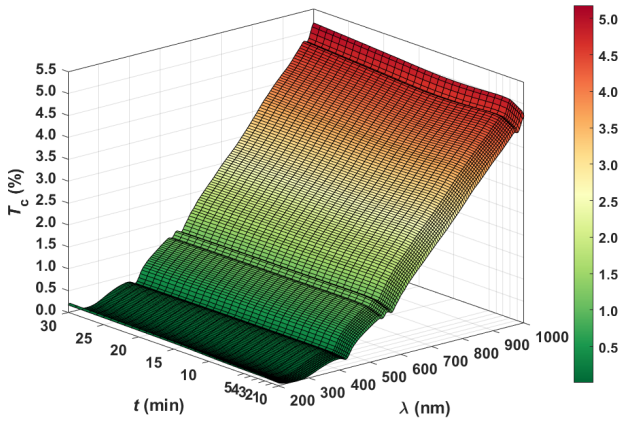

(a)

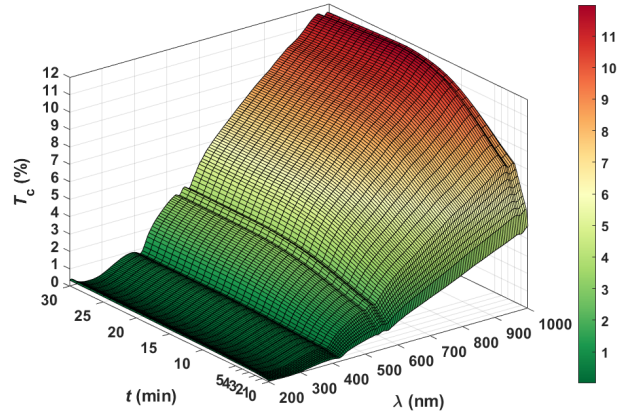

(b)

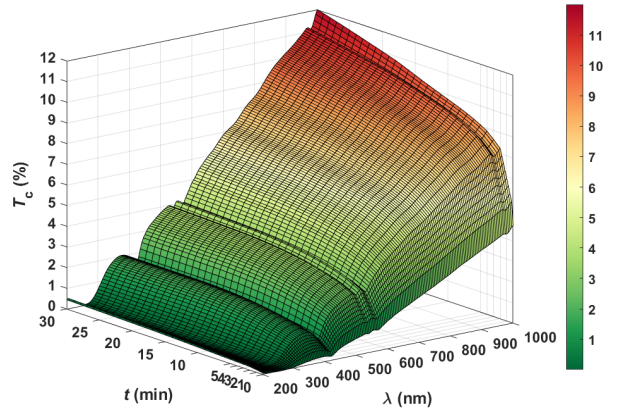

(c)

Fig. 8 Spectral T_c kinetics for colorectal muscle during treatments with: 20%-glycerol (a), 40%-glycerol (b) and 60%-glycerol (c).

To calculate the time dependence for $\mu_t(\lambda)$ in the three treatments, we used the thickness kinetics data from Fig. 6 and the T_c kinetics data from Fig. 8 in the BBL equation (Eq. (3)). Fig. 9 presents such kinetics between 200 and 1000 nm.

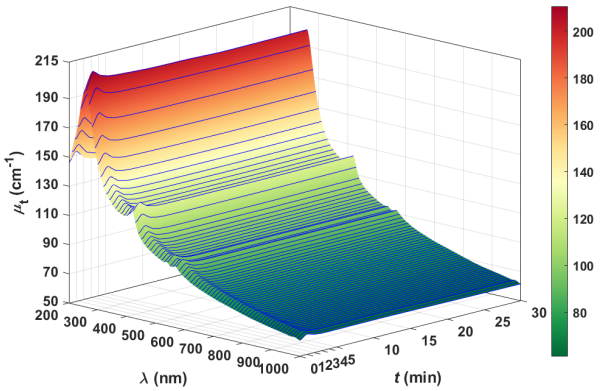

(a)

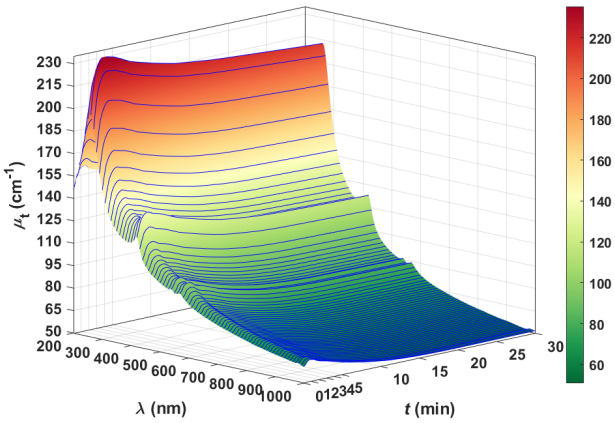

(b)

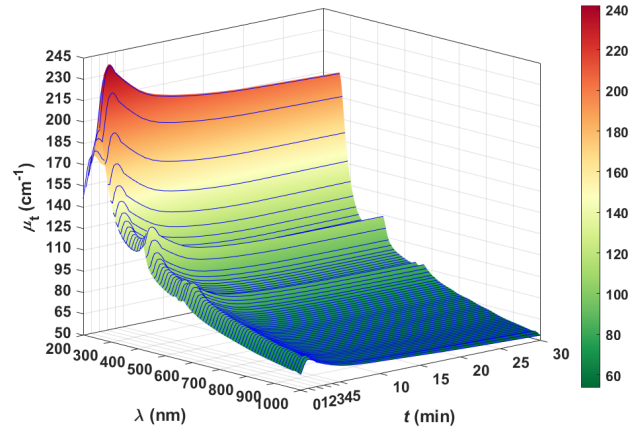

(c)

Fig. 9 Kinetics of $\mu_t(\lambda)$ for the treatments with: 20%-glycerol (a), 40%-glycerol (b) and 60%-glycerol (c).

All graphs in Fig. 9 show a fast increase in $\mu_t(\lambda, t)$ at the beginning of the treatment, followed by a smooth decrease. Such behavior is observed for the entire spectral range, but with higher magnitude in the UV. The magnitude of these variations also grows from treatment to treatment with the increase of glycerol concentration in the treating solution.

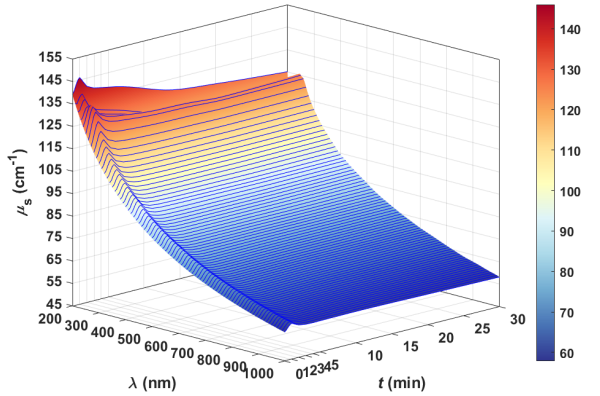

(a)

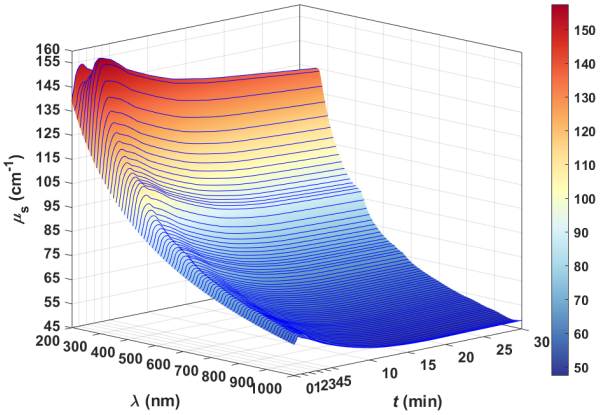

(b)

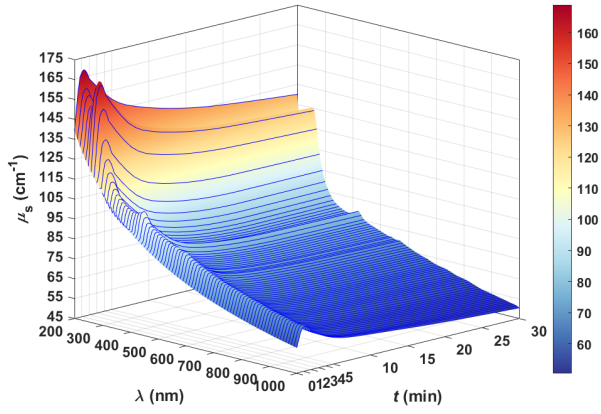

(c)

Fig. 10 Kinetics of $\mu_s(\lambda)$ for the treatments with: 20%-glycerol (a), 40%-glycerol (b) and 60%-glycerol (c).

By subtracting the unchanged $\mu_a(\lambda)$ (presented in Fig. 3) to $\mu_t(\lambda, t)$, we obtained $\mu_s(\lambda, t)$. Those graphs are presented in Fig. 10.

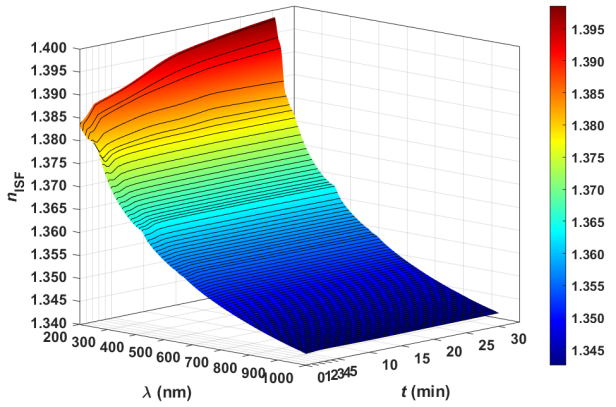

(a)

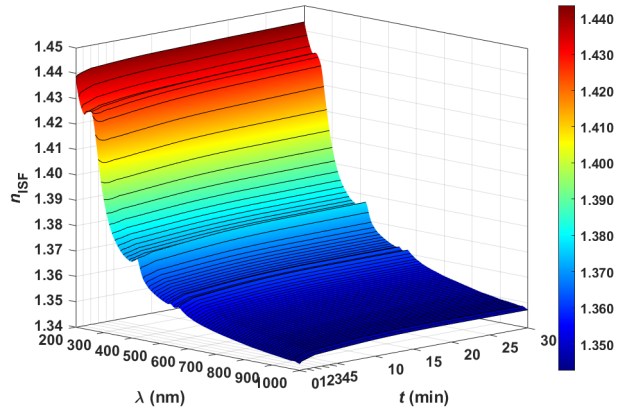

(b)

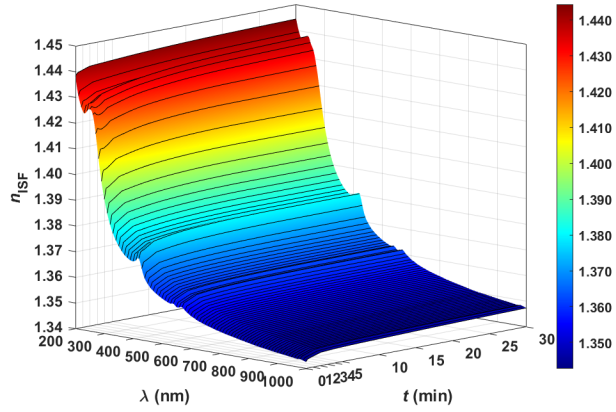

(c)

Fig. 11 Kinetics of $n_{ISF}(\lambda)$ for the treatments with: 20%-glycerol (a), 40%-glycerol (b) and 60%-glycerol (c).

Similarly to what was observed in the kinetics of $\mu_t(\lambda)$, $\mu_s(\lambda,t)$ also shows a fast increase at the beginning of the treatment, which indicates the approach of tissue

scatterers as a result of dehydration. Such increase is followed by a smooth decrease as a result of the RI matching mechanism. Once again the magnitude of these variations grows with the glycerol concentration in the treating solution. For the treatments with 40%- and 60%-glycerol we see that these variations also occur for the wavelengths that correspond to the hemoglobin bands, with the later treatment showing the highest magnitude for these variations. Due to the presence of the absorption bands of proteins (200–230 nm) and DNA (260 nm), if we consider a particular time of treatment, no smooth decay is observed for the $\mu_s(\lambda)$.

Using the dispersion of scatterers (top curve in Fig. 5), the thickness kinetics data in Fig. 6 and the kinetics for $\mu_s(\lambda)$ in graphs of Fig. 10 in Eq. (13), the time dependence for $n_{ISF}(\lambda)$ was calculated for the three treatments. Fig. 11 presents the results of this calculation.

As a result of the partial replacement of water by glycerol in the interstitial locations, the average RI of the ISF increases during treatment. According to all graphs in Fig. 11, such RI matching is stronger in the UV range, as expected, especially for wavelengths between 200 and 320 nm (red and orange areas). A comparison between the graphs in Fig. 11 shows that such RI matching in the UV presents a growing magnitude with increasing glycerol concentration in the treating solution. Such information is important for the development of future diagnostic/treatment procedures that will work at UV wavelengths.

Finally, combining the scatterers dispersion in Fig. 5 with the data in the three graphs of Fig. 11 in the Gladstone and Dale law (Eq. (7)), we have calculated the RI kinetics for the whole muscle. The resulting graphs of this calculation are presented in Fig. 12.

The kinetics presented in graphs of Fig. 12 are similar to the ones presented in graphs of Fig. 11, but now showing three clear stages: the dehydration mechanism is observed with the strong increase within the first min; a transition between the dehydration and RI matching mechanisms is observed in the following 3 min; and the RI matching mechanism dominates in the remaining 26 min. These graphs are clearer in showing that the magnitude in the RI increase is higher in the UV range and that such magnitude grows with increasing glycerol concentration in the treating solutions. Similar kinetics is seen for the absorption bands of proteins (200 nm), DNA (260 nm) and hemoglobin (418, 540, and 570 nm), meaning that the fraction of these biological molecules that were dissolved in the ISF are also subject of clearing.

4 Conclusion

The RI kinetics of human colorectal muscle were calculated based only on thickness and T_c measurements made during OC treatments with different glycerol osmolarities. To evaluate the RI matching mechanism between 200 and 1000 nm, the three treatments used in this study were performed with aqueous solutions of glycerol, where the water content was higher (20%-glycerol), equal (40%-glycerol) or smaller (60%-glycerol) than the mobile water content in the muscle. As part of the calculations, the kinetics for $\mu_s(\lambda)$ were also obtained, showing a decrease over the time of treatment as a result of the RI matching mechanism (see Fig. 11).

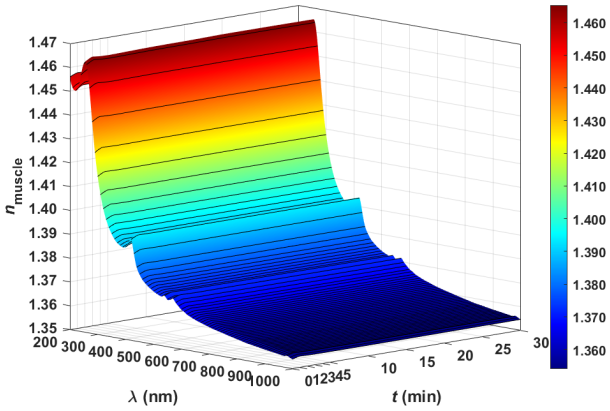

(a)

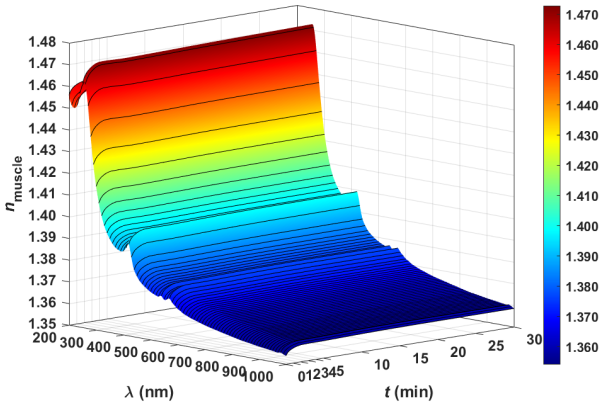

(b)

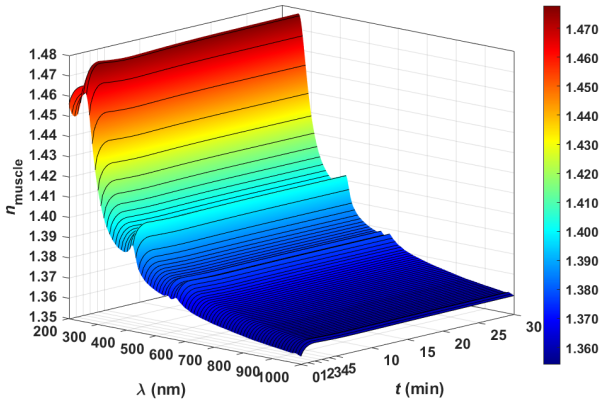

(c)

Fig. 12 Kinetics of $n_{muscle}(\lambda)$ for the treatments with: 20%-glycerol (a), 40%-glycerol (b) and 60%-glycerol (c).

It was observed that the smooth decreasing wavelength dependence was kept unchanged in all

treatments for μ_s, n_{ISF} and n_{muscle} between ~270 and 1000 nm. For shorter wavelengths, no smooth decrease wavelength dependence was observed during treatments due to the presence of the absorption bands of proteins and DNA. The kinetics observed in this wavelength range for μ_s and n_{ISF} are also slightly different than what was observed for higher wavelengths, which indicates that glycerol has dissolved protein and DNA molecules located in the ISF. Increase in n_{ISF} and n_{muscle} at 418, 540, and 570 nm, especially for the treatments with 40%-glycerol and 60%-glycerol, shows that some hemoglobin in the ISF might also be cleared.

Considering the visible-NIR range and the treatment with 40%-glycerol, the kinetics of n_{ISF} presented the expected smooth-increasing time dependence, which indicates the unique glycerol flux into the interstitial locations as a result of the water balance between the solution and the mobile water in the muscle. For the other treatments, such time dependence also shows a global increase, but not with smooth kinetics due to the water unbalance between tissue and treating solution.

A comparison between the UV and visible-NIR ranges shows that the magnitude of the RI matching is higher in the UV and that such magnitude rises with the increase of glycerol in the treating solution.

Such results proof that native tissues have stronger light scattering properties in the UV range and that OC treatments through the RI matching mechanism are an effective way to reduce such scattering. Such information in conjunction with the discovery of two OC-induced windows in the UV range [37], opens the possibility to develop new diagnostic and treatment procedures with the use of UV light.

Disclosures

The authors declare that there are no conflicts of interest related to this article.

Acknowledgements

This research was supported by the Portuguese Grant FCT UIDB/04730/2020.

VVT was supported by the grant of the Russian Foundation of Basic Research #18-29-02060 MK.

References

1. V. V. Tuchin, I. L. Maksimova, D. A. Zimnyakov, I. L. Kon, A. H. Mavlutov, and A. A. Mishin, "Light propagation in tissues with controlled optical properties," Journal of Biomedical Optics 2(4), 401–407 (1997).
2. L. M. C. Oliveira, V. V. Tuchin, The Optical Clearing Method: A New Tool for Clinical Practice and Biomedical Engineering, Springer, Cham: Switzerland (2019).
3. L. Oliveira, M. I. Carvalho, E. Nogueira, and V. V. Tuchin, "Optical clearing mechanisms characterization in muscle," Journal of Innovative Optical Health Sciences 9(5), 1650035 (2016).
4. A. Yu. Sdobnov, M. E. Darvin, E. A. Genina, A. N. Bashkatov, J. Lademann, and V. V. Tuchin, "Recent progress in tissue optical clearing for spectroscopic application," Spectrochimica Acta Part A: Molecular and Biomolecular Spectroscopy 197, 216–229 (2018).
5. O. Semyachkina-Glushkovskaya, A. Abdurashitov, A. Dubrovsky, D. Bragin, O. Bragina, N. Shushunova, G. Maslyakova, N. Navolokin, A. Bucharskaya, V. V. Tuchin, J. Kurths, and A. Shirokov, "Application of optical coherence tomography for in vivo monitoring of the meningeal lymphatic vessels during opening of blood-brain barrier: mechanisms of brain clearing," Journal of Biomedical Optics 22(12), 121719 (2017).
6. T. Yu, Y. Qi, H. Gong, Q. Luo, and D. Zhu, "Optical clearing for multiscale biological tissues," Journal of Biophotonics 11(2), e201700187 (2018).
7. A. Yu. Sdobnov, V. V. Tuchin, J. Lademann, and M. E. Darvin, "Confocal Raman microscopy supported by optical clearing treatment of the skin – influence on collagen hydration," Journal of Physics D: Applied Physics 50(28), 285401 (2017).
8. D. Chen, N. Zeng, Q. Xie, H. He, V. V. Tuchin, and H. Ma, "Mueller matrix polarimetry for characterizing microstructural variation of nude mouse skin during optical clearing," Biomedical Optics Express 8(8), 3559–3570 (2017).
9. M. G. Ghosn, E. F. Carbajal, N. A. Befrui, V. V. Tuchin, and K. V. Larin, "Differential permeability rate and percent clearing of glucose in different regions in rabbit sclera," Journal of Biomedical Optics 13(2), 021110 (2008).
10. Q. L. Zhao, J. L. Si, Z. Y. Guo, H. J. Wei, H. Q. Yang, G. Y. Wu, S. S. Xie, X. Y. Li, X. Guo, H. Q. Zhong, and L. Q. Li, "Quantifying glucose permeability and enhanced light penetration in ex vivo human normal and cancerous esophagus tissues with optical coherence tomography," Laser Physics Letters 8(1), 71–77 (2011).
11. H. Ullah, E. Ahmed, and M. Ikram, "Monitoring of glucose levels in mouse blood with noninvasive optical methods," Laser Physics 24(2), 025601 (2014).
12. O. Zhernovaya, V. V. Tuchin, and M. J. Leahy, "Blood optical clearing studied by optical coherence tomography," Journal of Biomedical Optics 18(2), 26014 (2013).

13. P. Liu, Y. Huang, Z. Guo, J. Wang, Z. Zhuang, and S. Liu, "Discrimination of dimethyl sulfoxide diffusion coefficient in the process of optical clearing by confocal micro-Raman spectroscopy," Journal of Biomedical Optics 18(2), 20507 (2013).
14. L. M. Oliveira, M. I. Carvalho, E. Nogueira, and V. V. Tuchin, "The characteristic time of glucose Diffusion measured for muscle tissue at optical clearing," Laser Physics 23, 075606 (2013).
15. L. M. Oliveira, M. I. Carvalho, E. M. Nogueira, and V. V. Tuchin, "Diffusion characteristics of ethylene glycol in skeletal muscle," Journal of Biomedical Optics 20(5), 051019 (2015).
16. S. Carvalho, N. Gueiral, E. Nogueira, R. Henrique, L. Oliveira, and V. V. Tuchin, "Glucose diffusion in colorectal mucosa – a comparative study between normal and cancer tissues," Journal of Biomedical Optics 22(9), 091506 (2017).
17. K. V. Berezin, K. N. Dvoretski, M. L. Chernavina, V. V. Nechaev, A. M. Likhter, I. T. Shagautdinova, E. Yu. Stepanovich, O. N. Grechukhina, and V. V. Tuchin, "Studying the mechanism of tissue optical clearing using the method of molecular dynamics," Proceedings of SPIE 10336, 103360J (2017).
18. K. V. Berezin, K. N. Dvoretski, M. L. Chernavina, A. M. Likhter, V. V. Smirnov, I. T. Shagautdinova, E. M. Antonova, E. Yu. Stepanovich, E. A. Dzhalmuhambetova, and V. V. Tuchin, "Molecular modeling of immersion optical clearing of biological tissues," Journal of Molecular Modeling 24(2), 45 (2018).
19. L. Pires, V. Demidov, I. A. Vitkin, V. S. Bagnato, C. Kurachi, and B. C. Wilson, "Optical clearing of melanoma in vivo: characterization by diffuse reflectance spectroscopy and optical coherence tomography," Journal of Biomedical Optics 21(8), 081210 (2016).
20. D. Abookasis, T. Moshe, "Reconstruction enhancement of hidden object using speckle contrast projections and optical clearing agents," Optics Communications 300, 58–64 (2013).
21. D. Zhu, W. Lu, Y. Weng, H. Cui, and Q. Luo, "Monitoring thermal-induced changes tumor blood flow and microvessels with laser speckle contrast imaging," Applied Optics 46(10), 1911–1917 (2007).
22. Y. Zhang, H. Liu, J. Tang, Z. Li, X. Zhou, R. Zhang, L. Chen, Y. Mao, and C. Li, "Non-invasively imaging subcutaneous tumor xenograft by handheld Raman detector, with assistance of optical clearing agent," ACS Applied Materials & Interfaces 9(21), 17769–17776 (2017).
23. M. Oldham, H. Sakhalkar, T. Oliver, M. Y. Wang, J. Kirkpatrick, J. Cao, C. Badea, and M. Dewhirst, "Three-dimensional imaging of xenograft tumors using optical computed and emission tomography," Medical Physics 33(9), 3193–3202 (2006).
24. M. Oldham, H. Sakhalkar, T. Oliver, G. A. Johnson, and M. Dewhirst, "Optical clearing of unsectioned specimens for three-dimensional imaging via optical transmission and emission tomography," Journal of Biomedical Optics 13(2), 021113 (2008).
25. M. Wei, L. Shi, Y. Shen, Z. Zhao, A. Guzman, L. J. Kaufman, L. Wei, and W. Min, "Volumetric chemical imaging by clearing-enhanced stimulated Raman scattering microscopy," Proceedings of the National Academy of Sciences 116(14), 6608–6617 (2019).
26. T. Lagerweijt, S. A. Dusoswa, A. Negrean, E. M. L. Hendrikx, H. E. Vries, J. Kole, J. J. Garcia-Vallejo, H. D. Mansvelder, W. P. Vandertop, D. P. Noske, B. A. Tannous, R. J. P. Musters, Y. van Kooyk, P. Wesseling, X. W. Zhao, and T. Wurdinger, "Optical clearing and fluorescence deep-tissue imaging for 3D quantitative analysis of the brain tumor microenvironment," Angiogenesis 20(4), 533–546 (2017).
27. J. Hirshburg, B. Choi, J. S. Nelson, and A. T. Yeh, "Collagen solubility correlates with skin optical clearing," Journal of Biomedical Optics 11(4), 040501 (2006).
28. V. Hovhannisyan, P.-S. Hu, S.-J. Chen, C.-S. Kim, and C.-Y. Dong, "Elucidation of the mechanisms of optical clearing in collagen tissue with multiphoton imaging," Journal of Biomedical Optics 18(4), 046004 (2013).
29. I. Costantini, R. Cicchi, L. Silvestri, F. Vanzi, and F. S. Pavone, "In-vivo and ex-vivo optical clearing methods for biological tissues: review," Biomedical Optics Express 10(10), 5251–5267 (2019).
30. E. A. Genina, A. N. Bashkatov, and V. V. Tuchin, "Tissue optical immersion clearing," Expert Review of Medical Devices 7(6), 825–842 (2010).
31. I. Carneiro, S. Carvalho, R. Henrique, L. Oliveira, and V. Tuchin, "Measurement of optical properties of normal and pathological human liver tissue from deep-UV to NIR," Proceedings of SPIE 11363, 113630D (2020).
32. H. Ding, J. Q. Lu, W. A. Wooden, P. J. Kragel, and X. H. Hu, "Refractive indices of human skin tissues at eight wavelengths and estimated dispersion relations between 300 and 1600 nm," Physics in Medicine and Biology 51(6), 1479–1489 (2006).
33. Z. Deng, J. Wang, Q. Ye, T. Sun, E. Zhou, J. Mei, C. Zhang, and J. Tian, "Determination of continuous complex refractive index dispersion of biotissue based on internal reflection," Journal of Biomedical Optics 21(1), 015003 (2016).
34. S. Liu, Z. Deng, J. Li, J. Wang, N. Huang, R. Cui, Q. Zhang, J. Mei, E. Zhou, C. Zhang, Q. Ye, and J. Tian, "Measurement of the refractive index of whole blood and its components for a continuous spectral region," Journal of Biomedical Optics 24(3), 035003 (2019).
35. Y. Zhou, J. Yao, and L. V. Wang, "Tutorial on photoacoustic tomography," Journal of Biomedical Optics 21(6), 061007 (2016).

36. P. Brescia, Micro-volume purity assessment of nuclei acids using A260/A280 ratio and spectral scanning protein and nucleic acid quantification (accessed: May 2020).
37. I. Carneiro, S. Carvalho, R. Henrique, L. Oliveira, and V. Tuchin, "Moving tissue spectral window to the deep-ultraviolet via optical clearing," Journal of Biophotonics 12(12), e201900181 (2019).
38. A. Yeh, B. Choi, J. S. Nelson, and B. J. Tromberg, "Reversible dissociation of collagen in tissues," Journal of Investigative Dermatology 121, 1332–1335 (2003).
39. L. M. Oliveira, M. I. Carvalho, E. M. Nogueira, and V. V. Tuchin, "Skeletal muscle dispersion (400-1000 nm) and kinetics at optical clearing," Journal of Biophotonics 11(1), e201700094 (2018).
40. V. V. Tuchin, Tissue Optics: Light Scattering Methods and Instruments for Medical Diagnosis, 3rd ed., SPIE Press, Bellingham (2015).
41. S. L. Jacques, "Optical properties of biological tissues: a review," Physics in Medicine and Biology 58(11), R37–R61 (2013).
42. J. Grienger, H. Groβ, J. Newkammer, and M. Bär, "Determining the refractive index of human hemoglobin solutions by Kramers-Kronig relations with an improved absorption model," Applied Optics 55(31), 8951–8961 (2016).
43. O. Sydoruk, O. Zhernovaya, V. Tuchin, and A. Douplik, "Refractive index of solutions of human hemoglobin from the near-infrared to the ultraviolet range: Kramers-Kronig analysis," Journal of Biomedical Optics 17(11), 115002 (2012).
44. I. Carneiro, S. Carvalho, R. Henrique, L. Oliveira, and V. V. Tuchin, "Kinetics of optical properties of colorectal muscle during optical clearing," IEEE Journal of Selected Topics in Quantum Electronics 25(1), 7200608 (2019).
45. V. V. Tuchin, Optical Clearing of Tissues and Blood, SPIE Press, Bellingham (2006).
46. I. Carneiro, S. Carvalho, V. Silva, R. Henrique, L. Oliveira, and V. V. Tuchin, "Kinetics of optical properties of human colorectal tissues during optical clearing: a comparative study between normal and pathological tissues," Journal of Biomedical Optics 23(12), 121620 (2018).
47. L. Oliveira, A. Lage, M. Pais Clemente, and V. V. Tuchin, "Optical characterization and composition of abdominal wall muscle from rat," Optics and Lasers in Engineering 47, 667–672 (2009).
48. L. Oliveira, A. Lage, M. Pais Clemente, and V. V. Tuchin, "Rat muscle opacity decrease due to the osmosis of a simple mixture," Journal of Biomedical Optics 15(5), 055004 (2010).
49. K. M. Meek, S. Dennis, and S. Khan, "Changes in the refractive index of the stroma and its extrafibrillar matrix when the cornea swells," Biophysical Journal 85(4), 2205–2212 (2003).
50. K. M. Meek, D. W. Leonard, C. J. Connon, S. Dennis, and S. Khan, "Transparency, swelling and scarring in the corneal stroma," Eye 17(8), 927–936 (2003).
51. O. Zhernovaya, O. Sydoruk, V. V. Tuchin, and A. Douplik, "The refractive index of human hemoglobin in the visible range," Physics in Medicine and Biology 56(13), 4013–4021 (2011).
52. E. N. Lazareva, V. V. Tuchin, "Measurement of refractive index of hemoglobin in the visible/NIR spectral range," Journal of Biomedical Optics 23(3), 035004 (2018).
53. E. N. Lazareva, V. V. Tuchin, "Blood refractive index modeling in the visible and near infrared spectral regions," Journal of Biomedical Photonics & Engineering 4(1), 010503 (2018).
54. I. Yu. Yanina, E. E. Lazareva, and V. V. Tuchin, "Refractive index of adipose tissue and lipid droplet measured in wide spectral and temperature ranges," Applied Optics 57(17), 4839–4848 (2018).
55. M. Daimon, A. Masumura, "Measurement of the refractive index of distilled water from the near-infrared region to the ultraviolet region," Applied Optics 46, 3811–3820 (2007).